ELSEVIER

Contents lists available at ScienceDirect

# **Materials Today Communications**

journal homepage: www.elsevier.com/locate/mtcomm





# First-principles calculation of stacking fault energies in Ni<sub>2</sub>(Cr, Mo)

Jie Song, Yao Fu

Department of Aerospace and Ocean Engineering, Virginia Tech, United States

ARTICLE INFO

Keywords: Ni<sub>2</sub>(Mo,Cr) Coherent precipitate General stacking fault energies Strengthening

#### ABSTRACT

The possible slip systems in  $Ni_2Cr$ ,  $Ni_2Mo$  and  $Ni_4MoCr$ , which are the main types of precipitates in technically important Ni-based alloys, are investigated using density functional theory-based calculations. The 12 most common slip systems, which are further reduced to four distinct systems due to the symmetry of the precipitate, are considered. The most and least favorable slip system have been identified through the general stacking fault energies analysis, which paves the way to further understand the strengthening mechanisms in the alloys containing these and similar types of precipitates.

#### 1. Introduction

Ni-based superalloys have been widely used in high temperature oxidative/corrosive environments, such as gas turbine engines, high temperature thermal energy storage nuclear power system and solar power plants. Amongst the Ni alloys, the Ni-Mo-Cr alloys like Haynes 242, Ni-W-Cr alloys like Haynes 230, and Ni-W-Cr-Mo alloys like Haynes 244 and Alloy 22 display better corrosion resistance [1,2]. These alloys derive their strength mainly from the long-range ordering reactions during heat treatment. In Alloy 22 and Haynes 242, ordered Ni<sub>2</sub>Cr (or Ni<sub>2</sub>(Cr,Mo)-type domains are responsible for the enhanced strength compared to un-aged alloys. The addition of Mo also contributes to higher solid solution strengthening, and extends the stability of the Ni<sub>2</sub>Cr phase to higher temperatures (~725 °C in Haynes 242). The low diffusion coefficients of Mo also contributes to a lower creep rate [3,4].

 $Ni_2(Mo,Cr)$  in the form of precipitates of size 10–100 nm [5,6] has been studied mainly as a strengthening phase in the nickel-based alloys. Due to the small size of the precipitates and difficulties to prepare bulk samples of  $Ni_2(Mo,Cr)$ , their physical and mechanical properties are challenging to be measured accurately. The ab-initio based computational methods can thus serve as a useful alternative [7–9]. The lattice parameters, elastic constants, and theoretical stress-strain curves of  $Ni_2Cr$  and  $Ni_2Mo$  have been computed by Chan et al. [7] using first-principles based approach. The computed materials properties are then used as input to estimate the tensile ductility and fracture toughness [7]. Bai et al. [8] discussed the stability of  $Ni_2Cr_{0.5}Mo_{0.5}$  by

computing the energy of formation of various  ${\rm Ni_2Cr_{1-x}Mo_x}$  alloys using density-functional theory calculations. Despite these efforts, the stacking faults (GSFs) in  ${\rm Ni_2(Mo,Cr)}$ , which play critical roles in the plastic deformation and strengthening, have not been studied in the past.

The Ni-rich matrix and Ni<sub>2</sub>(Mo,Cr) precipitates have the coherent relationship. During deformation, the alloys will be strengthened through shearing by pairs of superdislocations separated by stacking faults (antiphase boundaries) that hinders further dislocation motion. Therefore, stacking fault energies (SFEs) play key roles in the plastic deformation and strengthening of the alloys, which motivates our study. In this work, we will conduct the generalized stacking fault (GSF) energy analysis, a methodology established by Vitek [10], in Ni<sub>2</sub>Cr, Ni<sub>2</sub>Mo and Ni<sub>4</sub>MoCr (Ni<sub>2</sub>Mo<sub>0.5</sub>Cr<sub>0.5</sub>) alloys at 0 K via density function theory. The obtained intrinsic and unstable SFEs will be analyzed in terms of their respective roles in the strengthening mechanism.

## 2. Crystal structure and computational modeling procedure

## 2.1. Crystal structure

 $Ni_2(Mo,Cr)$  has a  $Pt_2Mo$  type or ordered orthorhombic structure. The crystallographic relationship between the  $Pt_2Mo$  structure and face-centered-cubic (FCC) matrix is shown in Fig. 1a [11,12]. Note  $Ni_2Cr$  ( $Pt_2Mo$  structure belongs to *Immm* space group<sup>1</sup>) is a stable phase with a disordering temperature of  $\sim 550~^{\circ}C$ , but  $Ni_2Mo$  is metastable [13]. The lattice parameters of the  $Ni_2(Mo,Cr)$  precipitates can thus be estimated

E-mail address: yaof@vt.edu (Y. Fu).

 $<sup>^{\</sup>star}$  Corresponding author.

<sup>&</sup>lt;sup>1</sup> The Ni<sub>4</sub>MoCr space group is *Pmmm* if the Cr atoms locate in Wyckoff a, Mo in h, and Ni in i and l positions, while Ni<sub>2</sub>(Mo,Cr) space group is *Immm* if the Cr and/or Mo atoms located randomly in Wyckoff a, and Ni in e positions. It is worth to mention here, the difference between Ni<sub>4</sub>MoCr and Ni<sub>2</sub>(Mo, Cr) is higher ordering in Ni<sub>4</sub>MoCr structure.

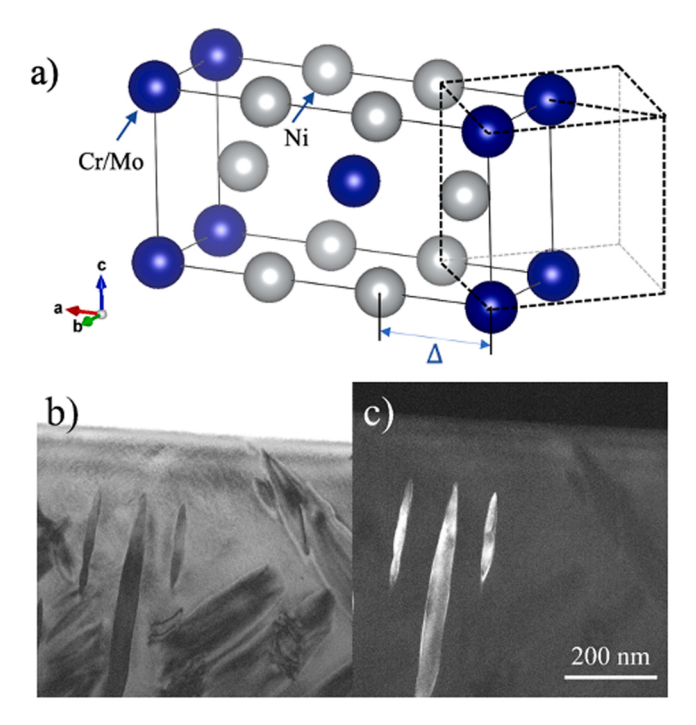


Fig. 1. (a) Schematic of crystallographic relationship between  $Pt_2Mo$  structure (solid line) and FCC matrix (dashed line); (b) and (c) centered bright field and dark field images of the  $Ni_2(Mo,Cr)$  precipitate in a Haynes 244 alloy viewed parallel to the habit plane showing the lenticular shape.

from the matrix lattice parameter as  $a_P = 3/\sqrt{2}a_M$ ,  $b_P = 1/\sqrt{2}a_M$ , and  $c_P = a_M$ , where subscript 'P' denotes the precipitate and 'M' denote the matrix (Fig. 1). There are a total of 6 possible correspondence variants (definition in ref 14).

The actual lattice parameters for the precipitates will deviate slightly from these values, that leads to the lattice mismatch. In the authors' previous studies, the Ni<sub>2</sub>(Mo,Cr) precipitates in Haynes 244 have been observed to be fully coherent with the Ni matrix and have a lenticular-shaped morphology [15–17]. The TEM images of Ni<sub>2</sub>(Mo,Cr) precipitates are shown in Fig. 1b and c. It can be observed that the Ni<sub>2</sub>(Mo,Cr) precipitates are fully coherent with the Ni matrix and form in a lenticular-shaped morphology, with the broad faces parallel to the  $\{110\}_M$  habit planes of the matrix and the  $(010)_P$  plane of Ni<sub>2</sub>(Mo,Cr) precipitate. This indicates that the lattice mismatch on the  $(010)_P$  plane of Ni<sub>2</sub>(Mo,Cr).

## 2.2. Slip system

The slip systems of coherent Ni<sub>2</sub>(Mo,Cr) precipitate are determined based on that 1) the precipitates are coherent with the matrix, 2) the matrix FCC structure has  $12 \{111\}_M \langle 110 \rangle_M$  slip systems. Therefore, the coherent Ni<sub>2</sub>(Mo,Cr) precipitate also have 12 slip systems. These 12 slip systems can be reduced to 4 distinct systems due to the *mmm* symmetry of Ni<sub>2</sub>(Mo,Cr) structure, as shown in Fig. 2 (slip planes are shaded, slip directions are shown as arrows of magnitude equal to  $1/2 \langle 110 \rangle_M$  dislocation).

# 2.3. Calculation details

# 2.3.1. Equilibrium lattice parameters calculation

 ${
m Ni_2Cr}$  and  ${
m Ni_2Mo}$  have an orthorhombic unit cell that contains six atoms per unit cell (four Ni atoms sit in the Wyckoff  $\underline{e}$  position and two Cr or two Mo atoms sit in the  $\underline{a}$  position) [18,19] (Fig. 1a). The unit cell of Ni<sub>4</sub>MoCr is constructed with the Cr atom placed to the corner and Mo atom placed to the center of the cell (Pmmm space group, Cr in a, Mo in

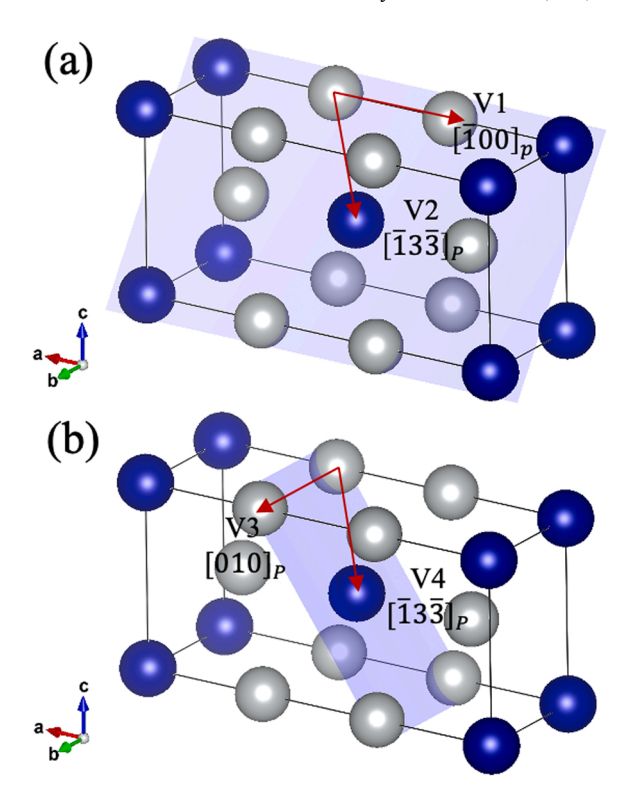


**Fig. 2.** (a, b) Four distinct slip systems (V1-V4) of Ni<sub>2</sub>(Mo,Cr) with orientation relationship to disordered FCC.

 $\underline{h}$ , and Ni in  $\underline{i}$  and  $\underline{l}$  positions) (Fig. 1a). Before computing the stacking fault energies, the total energies of Ni<sub>2</sub>Cr, Ni<sub>2</sub>Mo and Ni<sub>4</sub>MoCr at 0 K are computed first. Calculations were performed using the Vienna Ab Initio Simulation Package (VASP) [20] with the projected augmented wave (PAW) potentials that uses the plane wave basis set to expand the total wavefunctions. The cut-off energy  $E_{\rm cut}$  is chosen as 400 eV. Further increase the cut-off energy is found to lead to little change in the calculated values. The Fourier space sampling employs  $15 \times 15 \times 15$  k-points mesh by the Monkhorst-Pack scheme to ensure a stable convergence and high accuracy. The spin-polarization is turned on to allow for the magnetic state of Ni. All structures are relaxed until the self-consistent electronic energy for each ionic step converges to below  $10^{-8}$  eV.

The equilibrium lattice parameters are calculated by computing the total energy at different unit cell volume. The lattice parameters  $a,\,b,\,$  and  $c,\,$  and the shape of the unit cell is allowed to relax, using the reported value by Chan et al. [7] as the starting point. Two sequential sets of energy minimization have been conducted for each condition in order to obtain more accurate energy values: 1) With the cell volume fixed, the cell shape is first optimized with the atoms allowed to relax; 2) The total energy is computed again for optimized lattice atom positions in step 1 with both the cell volume and shape fixed. Around the lowest energy, the unit cell volume change is as small as 0.001% to obtain the accurate lattice parameters.

# 2.3.2. SFE calculation

To calculate the SFEs of V1 and V2 slip systems, a  $1 \times 1 \times 2$  supercell containing 6 layer is created with c along the  $[021]_P$  direction and the slip plane as  $(011)_P$ . A supercell slab+vacuum geometry is employed, where a vacuum is created with the periodic boundary conditions. The stacking of the Ni<sub>2</sub>(Mo,Cr) can be represented as ABC as shown in Fig. 3a, where the atom positions of different layers are represented by different letters. A 6 layers (approximately 14.5 Å) vacuum region is included along the cell's z axis. The stacking fault can be generated by displacing the 4–6th layers of the crystal through a fault vector along the V1  $[\overline{100}]_P$  and V2  $[\overline{133}]_P$  directions.

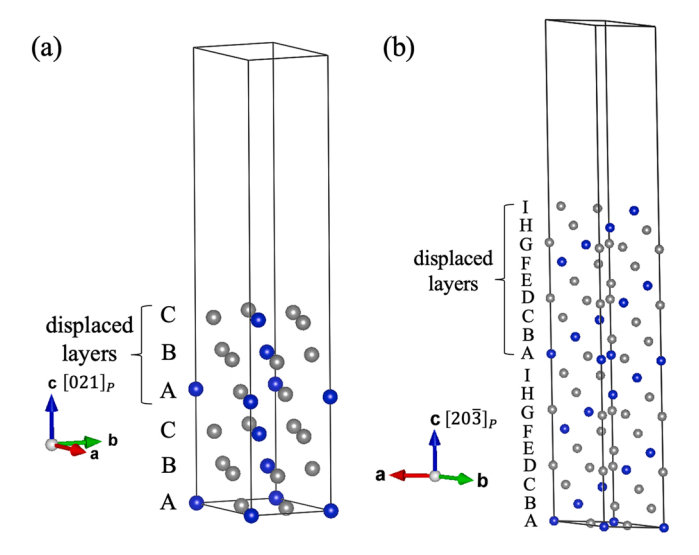


**Fig. 3.** Stacking sequence along the slip plane normal direction of (a) V1 and V2 slip system and (b) V3 and V4 slip systems.

Similarly, a  $1\times 1\times 2$  supercell containing 18 layers is created to calculate the SFEs of V3 and V4 slip system, with c along the  $[20\overline{3}]_p$  direction and the slip plane as  $(\overline{3}01)_p$ . The 6-layer vacuum region ( $\sim 14$  Å) is included along the cell's c axis. The stacking of the atoms can be represented as ABCDEFGHI as shown in the Fig. 3b, where the atom positions of different layers are represented by different letters. The stacking faults are generated by displacing the 10–18th layers of the crystal through a fault vector along the V3  $[010]_p$  and V4  $[\overline{1}3\overline{3}]_p$  directions.

## 3. Results and discussion

## 3.1. Computation of lattice parameters

The energies of formation are computed based on the difference between the total energy of the unit cell and the composition weighted average energy of the ferromagnetic fcc Ni (–5.4827 eV/atom) and bcc Mo (–10.8271 eV/atom). The energy of formation per mole of Ni<sub>2</sub>Cr, Ni<sub>2</sub>Mo and Ni<sub>4</sub>MoCr as a function of the unit cell volume is plotted in Fig. 4. A summary of the equilibrium parameter and the energy of formation are presented in Table 1, together with experimental data and other available theoretical results using first-principles based methods. The computed lattice parameters are in reasonably good agreement with the reported by Chan [7] and Arya [21]. The internal-structural

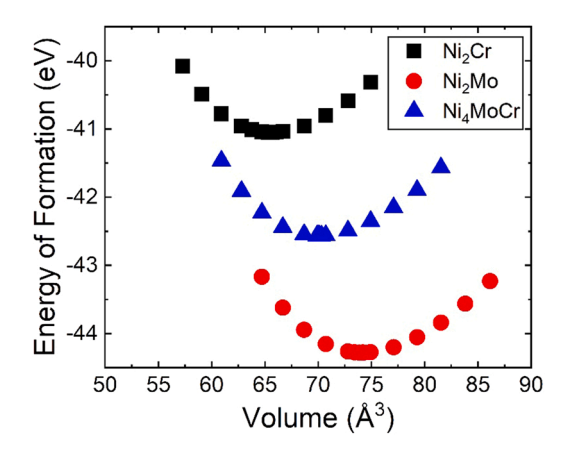


Fig. 4. Energy of formation of  $Ni_2Cr$ ,  $Ni_2Mo$ , and  $Ni_4MoCr$  cell as function of volume.

**Table 1**Summary of the Computed Lattice Constant, Internal-Structure Parameters and Energy Formation for Ni<sub>2</sub>(Mo,Cr) Compounds.

	Lattice Parameter			$\Delta - \frac{1}{3}$	Method	Reference	
Ni <sub>2</sub> Cr	a (Å)	b (Å)	c (Å)	- 3			
	7.423	2.476	3.568	0.000564	VASP	Present study	
	7.36	2.46	3.55	0.0001	WIEN2K	Chan et al.	
	7.48	2.49	3.53		WIEN97	Arya et al.	
$Ni_2Mo$	7.715	2.621	3.667	-0.002358	VASP	Present study	
	7.69	2.57	3.71	-0.0018	WIEN2K	Chan et al.	
	7.95	2.65	3.74		WIEN97	Arya et al.	
Ni <sub>4</sub> MoCr	7.595	2.555	3.609	-0.009924/ 0.005958 <sup>a</sup>	VASP	Present study	

 $<sup>^{\</sup>rm a}\,$  -0.009924 Å references to the Cr and 0.005958 Å references to Mo

parameter ( $\Delta$ ) is used to represent the distance from the Cr atom (or Mo atom) at the corner, and the deviation of Ni atom from the ideal position a/3 would be  $(\Delta-1/3)a$  (Fig. 1a). The computed equilibrium lattice parameters for 0 K shows a good agreement with that of the previous reported studies.

## 3.2. Stacking fault energy calculation

The stacking faults are first evaluated for Ni<sub>2</sub>Cr in the supercell setup (Fig. 3a). The SFEs are evaluated by displacing the top half of the supercell relative to the lower half through a fault vector along the V1 direction as indicated by the solid arrow of Fig. 5a. The intrinsic SFE at this local saddle point is calculated as  $\gamma_{sf} = (E_{sf} - E)/A$ , where  $E_{sf}$  and E are the energies of the structure with and without stacking fault that contains the same number of atoms. Here A is the stacking fault area.

The  $\gamma_{sf}$  at different k-points of system V1 in Ni<sub>2</sub>Cr are compared as listed in Table 2. The number of layers between stacking faults is also increased by creating a  $1 \times 1 \times 4$  supercell and displacing the 7–12th layers along V1. In the  $1 \times 1 \times 4$  supercell, there are 6 layers between

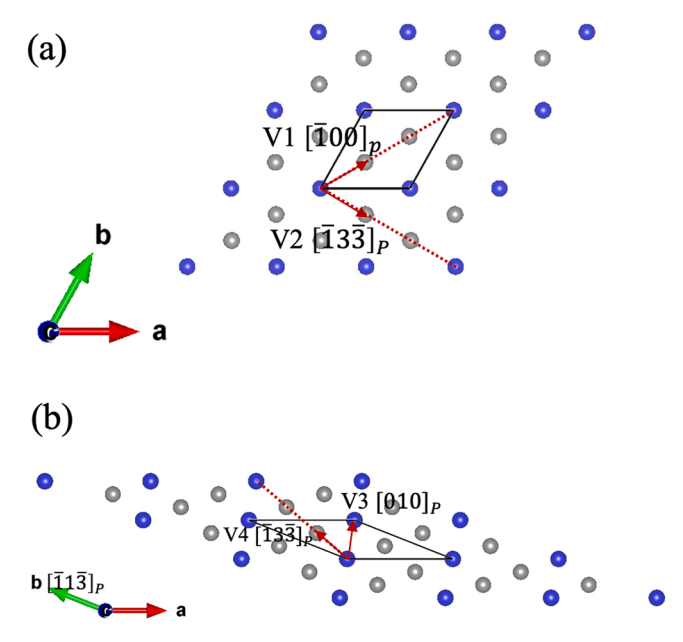


Fig. 5. Atom arrangement on the slip planes of  $Ni_2Cr$  and  $Ni_2Mo$ : (a) V1 and V2 slip systems and (b) V3 and V4 slip systems; slip directions on the slip planes are marked by arrows.

**Table 2** Calculated intrinsic stacking fault energy  $(\gamma_{isf})$  of Ni<sub>2</sub>Cr along V1 slip direction at different k-point and supercell size.

Supercell size	k-points	$\gamma_{isf} (mJ/m^2)$		
$1 \times 1 \times 2$	$9 \times 9 \times 1$	221.22		
$1 \times 1 \times 2$	$15\times15\times1$	224.76		
$1 \times 1 \times 2$	$19\times19\times1$	224.44		
$1 \times 1 \times 4$	$15\times15\times1$	232.06		

the stacking fault and vacuum. It can be observed that the SFE computed with  $1\times1\times2$  supercell at  $15\times15\times1$  k-points only differ from that obtained with the same geometry at  $19\times19\times1$  k-points by 0.13% and from that with the  $1\times1\times4$  supercell by 3.02%, demonstrating great convergence. Therefore, the  $1\times1\times2$  supercell (3 layers between stacking fault and vacuum) with  $15\times15\times1$  k-points is adopted for the calculation of V1 and V2 slip systems of Ni<sub>2</sub>Cr, Ni<sub>2</sub>Mo and Ni<sub>4</sub>MoCr.

In Ni<sub>2</sub>Cr or Ni<sub>2</sub>Mo, the primitive cell lattice vectors a and b on the slip plane of V1 and V2 slip systems are along  $[\overline{1}1\overline{1}]_p$  and  $[\overline{1}11]_p$ , respectively. The atom arrangements of the ab planes (slip planes) are shown in the Fig. 5a, where the stacking fault vector is indicated by the dashed lines. The primitive cell lattice vectors  $\mathbf{a}$  and  $\mathbf{b}$  on the slip plane of the V3 and V4 slip systems are along  $[1\overline{1}3]_p$  and  $[\overline{1}1\overline{3}]_p$ , respectively (Fig. 5b). Different from Ni<sub>2</sub>Cr or Ni<sub>2</sub>Mo primitive cell, the Ni<sub>4</sub>MoCr primitive cell has four Ni, one Mo, and one Cr, along the slip plane as showed in Fig. 6. The primitive cell lattice vector  $\mathbf{a}$  and  $\mathbf{b}$  on the slip plane of V1 and V2 slip system are along  $[0\overline{1}1]_p$  and  $[\overline{1}00]_p$ , respectively (Fig. 6a), while on the slip plane of V3 and V4, the  $\mathbf{a}$  and  $\mathbf{b}$  vectors are  $[010]_p$  and  $[103]_p$ , respectively (Fig. 6b). The supercells are presented in Fig. 3. The SFE profile as a function of stacking fault vector are presented in Fig. 7 to

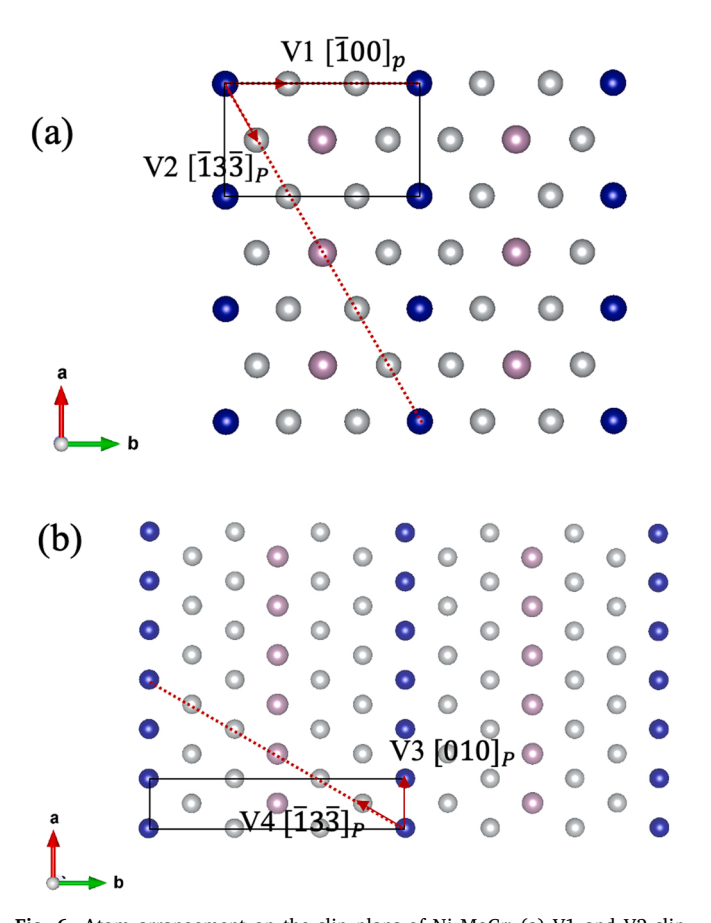


Fig. 6. Atom arrangement on the slip plans of  $\rm Ni_4MoCr$ : (a) V1 and V2 slip systems and (b) V3 and V4 slip systems; slip directions on the slip planes are marked by arrows.

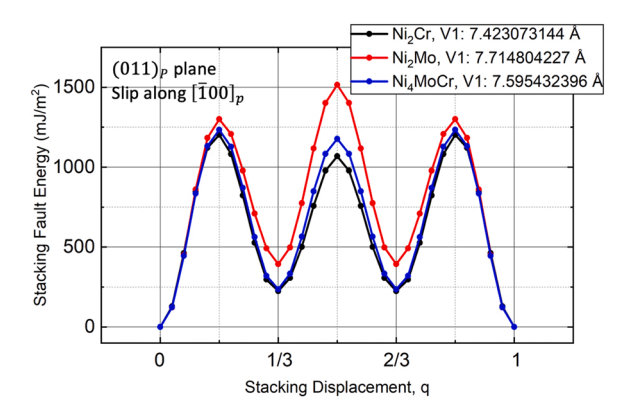


Fig. 7. Stacking fault energy profiles as a function of the fault vector for the V1 slip system; fault vectors are along the dashed line in Fig. 5a for Ni<sub>2</sub>Cr and Ni<sub>2</sub>Mo and along the dashed line in Fig. 6a for Ni<sub>4</sub>MoCr; the full displacement corresponding to the fault free structure, i.e., total length of the dashed line, is also listed in the figure legend.

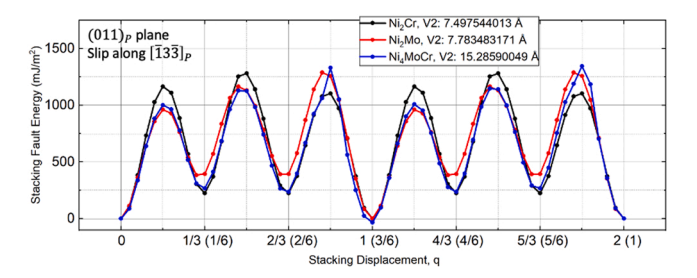


Fig. 8. Stacking fault energy profiles as a function of the fault vector for the V2 slip system; fault vectors are along the dashed line in Fig. 5a for Ni<sub>2</sub>Cr and Ni<sub>2</sub>Mo and along the dashed line in Fig. 6a for Ni<sub>4</sub>MoCr; the fault vectors for Ni<sub>4</sub>MoCr are in the parentheses; the full displacement corresponding to the fault free structure, i.e., total length of the dashed line, is also listed in the figure legend.

## Fig. 10.

The stable SFE, i.e., intrinsic SFE,  $\gamma_{isf}$  is the local energy minima, that affects the dislocation splitting width. The unstable SFE  $\gamma_{usf}$ , which is the local energy maximum, denotes the lowest energy barrier for dislocation nucleation [22]. In the case of V1, V2 and V4 for Ni<sub>2</sub>Cr and Ni<sub>2</sub>Mo, there are multiple local maximum and minimum values (e.g.,  $q = \frac{1}{6}, \frac{1}{3}, \frac{1}{2},$  etc) along the fault vector path, indicating multiple possible partial dislocations along the slip directions. For Ni<sub>4</sub>MoCr, the local maximum and minimum values are along multiples of  $q = \frac{1}{6}$  and  $q = \frac{1}{12}$  for V1 and V2/V4, respectively. Replacing Cr with Mo atoms does not alter the locations of local maximum and minimum SFE, but the magnitudes of SFE vary with Cr substitution with Mo. In V1, the SFE increases with Mo, most pronounced at  $q = \frac{1}{2}$  changing the maximum unstable  $\gamma_{usf}$  from q = $\frac{1}{6}$  in Ni<sub>2</sub>Cr and Ni<sub>4</sub>MoCr to  $q = \frac{1}{2}$  in Ni<sub>2</sub>Mo (Fig. 7). Similar increase in SFE can be observed for V3 but with a small magnitude (Fig. 9). It is worth mentioning that the SFE profile in V1 and V3 is symmetric respect to q = $\frac{1}{2}$  due to mmm symmetry. The SFE change with composition variation is more complicated in V2 and V4. While the  $\gamma_{usf}$  reduces at  $q = \frac{1}{6} \left( \frac{1}{12} \right)$  and  $\frac{1}{2}(\frac{1}{4})$  (the values in parathesis are for Ni<sub>4</sub>MoCr) with Mo replacing Cr in V2, the  $\gamma_{usf}$  at  $q = \frac{5}{6} \left( \frac{5}{12} \right)$  and  $\gamma_{isf}$  at  $q = \frac{1}{3} \left( \frac{1}{6} \right)$  and  $\frac{2}{3} \left( \frac{1}{3} \right)$  increase (Fig. 8). In the case of V4, the  $\gamma_{usf}$  and  $\gamma_{isf}$  increases dramatically at  $q = \frac{1}{2} \left( \frac{1}{4} \right)$  and  $q = \frac{1}{2} \left( \frac{1}{4} \right)$  $\frac{1}{3}(\frac{1}{6})$  for Ni<sub>2</sub>Mo, thus varying the SFE profiles (Fig. 10). In particular, the  $\gamma_{isf}$  at  $q = \frac{1}{3} \left( \frac{1}{6} \right)$  in Ni<sub>2</sub>Mo is higher than that at  $q = \frac{2}{3} \left( \frac{1}{3} \right)$ , thus making its stacking fault formation less stable, whereas the reverse is found for Ni<sub>4</sub>MoCr. In Ni<sub>2</sub>Cr, the  $\gamma_{isf}$  at  $q=\frac{1}{3}\left(\frac{1}{6}\right)$  and  $q=\frac{2}{3}\left(\frac{1}{3}\right)$  are comparable (Fig. 10).

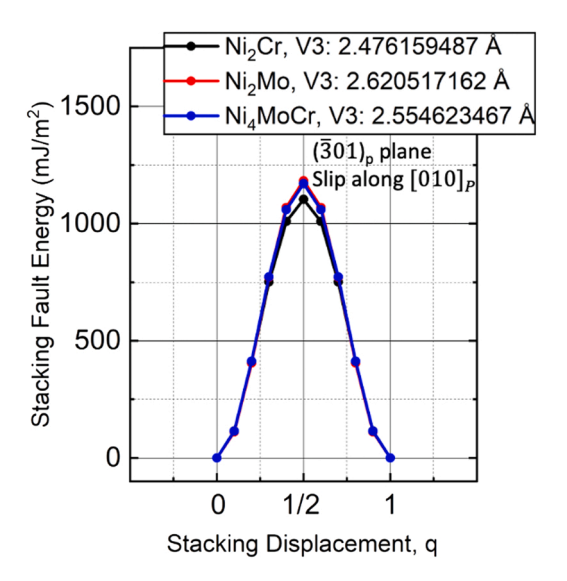


Fig. 9. Stacking fault energy profiles as a function of the fault vector for the V3 slip system; fault vectors are along the dashed line in Fig. 5b for  $Ni_2Cr$  and  $Ni_2Mo$  and along the dashed line in Fig. 6b for  $Ni_4MoCr$ ; the full displacement corresponding to the fault free structure, i.e., total length of the dashed line, is also listed in the figure legend.

The maximum unstable and minimum intrinsic SFE  $\gamma_{usf,max}$  and  $\gamma_{isf,min}$  are extracted from Fig. 7 to Fig. 10 and summarized in Table 3. The  $\gamma_{usf,max}$  differs among the different slip systems. In Ni<sub>2</sub>Cr, Ni<sub>2</sub>Mo, and Ni<sub>4</sub>MoCr, the  $\gamma_{usf,max}$  in the V3 direction is the lowest, thus is the most preferable slip direction among the four systems investigated. Moreover, there is no saddle point that corresponds to the intrinsic stacking fault in the V3 direction. The  $\gamma_{usf,max}$  in the V4 direction is the highest, making it most difficult to deform through shearing in that direction. Moreover, V1, V2, and V4 each has two (five) local minimum points in the energy profiles in Ni<sub>2</sub>Cr and Ni<sub>2</sub>Mo (Ni<sub>4</sub>MoCr), indicating multiple possible partial dislocations and higher chance of stacking fault formation during the slip process. Replacing Cr with Mo atoms lead to both changes in the

unstable stacking energy  $\gamma_{usf,max}$  and intrinsic stacking fault energy  $\gamma_{isf,min}$ , as shown in Table 3. In Ni<sub>2</sub>Mo, the  $\gamma_{usf,max}$  of V2 and V3 are comparably lower, making them the more favorable slip systems than V1 and V4. It is noted that the  $\gamma_{isf,min}$  is negative for V2 in Ni<sub>4</sub>MoCr indicating a very stable stacking fault at  $q=\frac{1}{2}$  corresponding to the fault-free structure in Ni<sub>2</sub>Mo and Ni<sub>2</sub>Cr.

Considering that the precipitates have six equivalent orientations with respect to the matrix, all slip systems could activate under the applied loading so that the strengthening effect would be the average of V1 to V4. However, it is also possible to achieve strengthening by forming single variant, in order to promote its activation which results in the strongest strengthening effect. The single variant can be formed during stress-aided aging and has been discussed in our previous work [17]. The increase in the yield strength in a certain loading direction may be achieved by selecting the precipitate variant of which the Schmid factor is largest, for example, V4 system, in order to promote its activation which results in the strongest strengthening effect. On the other hand, the slip system that has the largest Schmid factor may not be activated. Due to difference in the unstable stacking fault of the slip systems, the largest Schmid factor system may operate at even higher stress compared to the second or third largest Schmid factor systems. This will also lead to enhanced strengthening effect (the smaller the Schmid factor, the higher the required stress).

To investigate the effect of single variant formation on the initial yield stage, micro-pillars are machined using focused ion beam (FIB) from chosen grains of the polycrystalline samples so that each pillar is single crystalline. The samples are either solution heat treated (SHT) with no precipitation or stress-aged with selected variants. Compressive loading to the micropillars containing either no precipitates or single selected variant are then conducted (Fig. 11). In the SHT sample with no precipitates, it has been found that the first active slip system has the largest Schmid factor (the estimation is based on the crystal directions of the sample coordinates) (Fig. 11b). However, in single-variant pillar, the first active slip system does not have the largest Schmid factor (second largest instead) (Fig. 11d). This test has been conducted for multiple micro-pillars. The shortcoming of the micro-pillar compression methodology is the difficulty to extract reliable stress-strain relations and to perform post-deformation analysis using advanced characterization

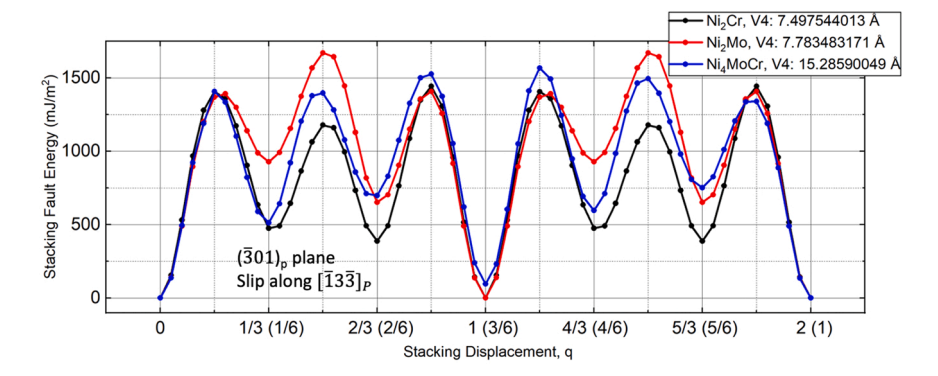
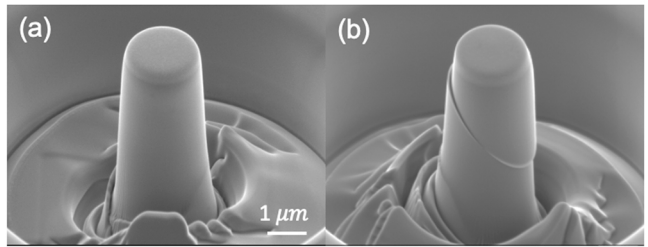


Fig. 10. Stacking fault energy profiles as a function of the fault vector for the V4 slip system; fault vectors are along the dashed line in Fig. 5b for  $Ni_2Cr$  and  $Ni_2Mo$  and along the dashed line in Fig. 6b for  $Ni_4MoCr$ ; the fault vectors for  $Ni_4MoCr$  are in the parentheses; the full displacements corresponding to the fault free structure, i.e., total length of the dashed line, are listed in the figure legend.

 $\label{eq:table 3} \textbf{Estimated stacking energies in mJ/m}^2 \ of \ different \ slip \ systems \ of \ Ni_2Cr, \ Ni_2Mo, \ and \ Ni_4MoCr.$ 

	V1 (011)[ <del>1</del> 00]			$\begin{array}{c} V2 \\ (011)[\overline{1}3\overline{3}] \end{array}$		V3 (301)[010]		V4 (301)[133]	
Type	$\gamma_{usf,max}$	$\gamma_{isf, \min}$	$\gamma_{usf, max}$	$\gamma_{isf, \min}$	$\gamma_{usf, \max}$	$\gamma_{isf, \min}$	$\gamma_{usf, max}$	$\gamma_{isf, \min}$	
Ni <sub>2</sub> Cr	1203	225	1281	225	1103	NA	1443	388	
Ni <sub>2</sub> Mo	1515	394	1288	384	1183	NA	1670	652	
Ni <sub>4</sub> MoCr	1234	237	1345	-34	1171	NA	1568	95	

# Compressive force direction [7 2 12]



# Compressive force direction $[\overline{3} \ 7 \ 14]$

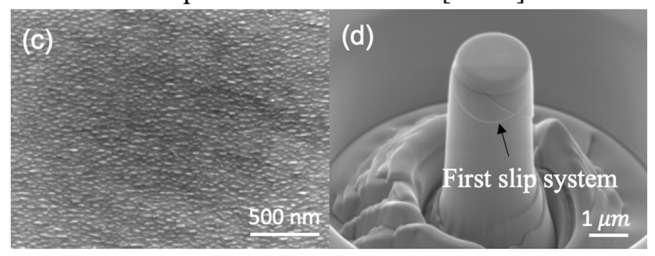


**Fig. 11.** (a) Focused ion beam (FIB) machined micro-pillar, (b) slip step shown in the SHT pillar after nanoindentation, (d) single-variant precipitates (shown in c) containing micro-pillar and its slip system after nanoindentation.

techniques so that the slip systems can be evaluated more accurately. Our future work thus includes fabricating centimeter-sized single crystal alloy and conduct mechanical loading on samples containing single or multiple variants under various temperatures to understand the deformation mechanism and clarifying the roles of the coherent  $\rm Ni_2(Mo,Cr)$  precipitates.

#### 4. Conclusion and future work

The possible slip systems in Ni<sub>2</sub>(Mo,Cr) have been investigated by calculating the GSF energy curves and extracting the intrinsic and unstable stacking fault energies using first principles calculations. The  $(\overline{3}01)\langle010\rangle$  precipitate slip system has been identified as the preferrable one, whereas the  $(\overline{3}01)\langle\overline{1}3\overline{3}\rangle$  as the least favorable one according to the analysis of the unstable stacking fault energy. The unstable and intrinsic stacking faults vary with the Mo replacing Cr atom and alter the most possible partial dislocations. These analyses are conducted based on the calculation of 0 K. Future work will consider the calculation at room and elevated temperatures that can provide more accurate guidance to the strengthening effect of the alloy containing Ni<sub>4</sub>MoCr precipitates. Moreover, more experimental evidence will be needed to provide the information of active slip systems in the precipitates and the resultant strengthening enhancement.

## **Declaration of Competing Interest**

The authors declare the following financial interests/personal relationships which may be considered as potential competing interests: Yao Fu reports financial support was provided by National Science Foundation

#### **Data Availability**

Data will be made available on request.

## Acknowledgements

The authors gratefully acknowledge the National Science Foundation (Award No. 2104941) for providing the financial support. The authors also acknowledge the Advanced Research Computing at Virginia Tech for providing computational resources and technical support that have contributed to the results reported within this paper.

#### References

- H. Sun, P. Zhang, J. Wang, Effects of alloying elements on the corrosion behavior of Ni-based alloys in molten NaCl-KCl-MgCl2 salt at different temperatures, Corros. Sci. 143 (2018) 187–199
- [2] J.W. Ambrosek, 2011. Molten Chloride Salts for Heat Transfer in Nuclear Systems Ph.D. thesis, The University of Wisconsin - Madison, (2011).
- [3] R. Tanaka, T. Kondo, Research and development on heat-resistant alloys for nuclear process heating in Japan, Nucl. Technol. 66 (1984) 75–87.
- [4] R. Watanabe, Y. Chiba, Effects of Cr-W balance and C content on structure and creep rupture strength in Ni-Cr-W alloy system, Tetsu-to-Hagane 65 (1979) 1013–1021
- [5] L. Yuan, R. Hu, T. Zhang, Y. Han, X. Xue, J. Li, Precipitation behavior of Pt2Mo-Type superlattices in hastelloy C-2000 superalloy with low Mo/Cr ratio, J. Mater. Eng. Perform. 23 (2014) 3314–3320.
- [6] M. Kumar, V.K. Vasudevan, Ordering reactions in an Ni25Mo8Cr alloy, Acta Mater. 44 (1996) 1591–1600.
- [7] K.S. Chan, Y.D. Lee, Y.M. Pan, First-principles computations of mechanical properties of Ni2Cr and Ni2Mo, Metall. Mater. Trans. A 37 (2006) 523–537.
- [8] J. Bai, Q. Zhan, X. Li, R. Yu, Enhanced stability of the strengthening phase Ni2(Cr, Mo) in Ni–Cr–Mo alloys by adjacent instability, Comput. Mater. Sci. 109 (2015) 111–114.
- [9] Y. Wang, C. Woodward, S.H. Zhou, Z.K. Liu, L.Q. Chen, Structural stability of Ni–Mo compounds from first-principles calculations, Scr. Mater. 52 (2005) 17–20.
- [10] V. Vitek, Structure of dislocation cores in metallic materials and its impact on their plastic behaviour, Prog. Mater. Sci. 36 (1992) 1–27.
- [11] S.K. Das, G. Thomas, The metastable phase Ni2Mo and the initial stages of ordering in Ni-Mo alloys, Phys. Status Solidi A 21 (1974) 177–190.
- [12] G. Van Tendeloo, Short range order considerations and development of long range order in different Ni-Mo alloys, Mater. Sci. Eng. 26 (1976) 209–220.
- [13] V.K. Vasudevan, E.E. Stansbury, C.R. Brooks, Domain coarsening at grain boundaries in ordered Ni4Mo, Acta Metall. Et. Mater. 40 (1992) 2113–2122.
- [14] Y. Gao, R. Shi, J.-F. Nie, S.A. Dregia, Y. Wang, Group theory description of transformation pathway degeneracy in structural phase transformations, Acta Mater. 109 (2016) 353–363.
- [15] J. Song, R. Field, M. Kaufman, Crystallography of grain boundary precipitates in a Ni-Mo-Cr-W low CTE alloy, J. Alloy. Compd. 702 (2017) 687–692.
- [16] J. Song, R. Field, D. Konitzer, M. Kaufman, Development of grain boundary precipitate-free zones in a Ni-Mo-Cr-W alloy, Metall. Mater. Trans. A 48 (2017) 2425–2434.
- [17] J. Song, R. Field, A. Clarke, Y. Fu, M. Kaufman, Variant selection of intragranular Ni2(Mo,Cr) precipitates (γ') in the Ni-Mo-Cr-W alloy, Acta Mater. 165 (2019) 362, 372
- [18] L. Karmazin, J. Krejčí, J. Zeman,  $\gamma$  Phase and Ni2Cr-type long-range order in Nirich NiCrMo alloys, Mater. Sci. Eng.: A 183 (1994) 103–109.
- [19] E. Gozlan, M. Bamberger, S.F. Dirnfeld, B. Prinz, J. Klodt, Topologically close-packed precipitations and phase diagrams of Ni-Mo-Cr and Ni-Mo-Fe and of Ni-Mo-Fe with constant additions of chromium, Mater. Sci. Eng.: A 141 (1991) 85–95.
- [20] G. Kresse, T. Demuth, F. Mittendorfer. VAMP/VASP, (http://cms.mpi.univie.ac.at/vasp/). (2003).
- [21] A. Árya, G.K. Dey, V.K. Vasudevan, S. Banerjee, Effect of chromium addition on the ordering behaviour of Ni–Mo alloy: experimental results vs. electronic structure calculations, Acta Mater. 50 (2002) 3301–3315.
- [22] H. Van Swygenhoven, P.M. Derlet, A.G. Frøseth, Stacking fault energies and slip in nanocrystalline metals, Nat. Mater. 3 (2004) 399–403.